

Classifying the Equation of State from Rotating Core Collapse Gravitational Waves with Deep Learning

Matthew C. Edwards

Department of Statistics, University of Auckland, Auckland, New Zealand

In this paper, we seek to answer the question “*given an image of a rotating core collapse gravitational wave signal, can we determine its nuclear equation of state?*”. To answer this question, we employ a deep convolutional neural network to learn visual patterns embedded within rotating core collapse gravitational wave (GW) signals in order to predict the nuclear equation of state (EOS). Using the 1824 rotating core collapse GW simulations by Richers et al [29], which has 18 different nuclear EOS, we consider this to be a classic multi-class image classification problem. We attain up to 71% correct classifications in the test set, and if we consider the “top 5” most probable labels, this increases to up to 97%, demonstrating that there is a moderate and measurable dependence of the rotating core collapse GW signal on the nuclear EOS.

I. INTRODUCTION

To date, gravitational waves (GWs) from stellar core collapse have not been directly observed by the network of terrestrial detectors, Advanced LIGO and Advanced Virgo [2]. However, they are a promising source [17], and we could learn a great deal about the dynamics of the core collapse, and the shock revival mechanism that leads to explosion [22]. It may even be possible to constrain the nuclear equation of state (EOS).

The death of massive stars (of at least $10 M_{\odot}$ at ZAMS) begins when the star exhausts its thermonuclear fuel through fusion, leaving an iron core that is supported by the pressure of relativistic degenerate electrons. Once the core reaches the Chandrasekhar limit, electron degeneracy pressure cannot support it, and collapse ensues. The core compresses, increasing in density, and squeezing protons and electrons together to create neutrons and neutrinos via electron-capture. The strong nuclear force halts the collapse by a stiffening of the nuclear EOS, which causes the inner core to rebound (or bounce), creating a shock wave that blasts into the in-falling outer core. The shock wave on its own is not strong enough to generate a supernova explosion, leading to a number of competing theories of the shock-revival such as the neutrino-driven mechanism and the magnetorotational mechanism [3, 9, 21, 22].

Inferring the supernova explosion (or shock-revival) mechanism has been the primary focus of the parameter estimation literature for core collapse GWs (see e.g., Chan et al [6], Logue et al [24], Powell et al [26, 27]) and this has naturally been treated

as a classification problem due to the competing mechanisms (namely, the neutrino mechanism and the magnetorotational mechanism) having distinct waveform morphologies. Other efforts have focused on estimating various parameters that have been noted to significantly influence a rotating core collapse GW waveform, such as the ratio of rotational kinetic energy to gravitational potential energy of the inner core at bounce, and the precollapse differential rotation profile [3, 11].

The nuclear EOS, however, is a poorly understood part of physics, though theoretical, experimental, and observational constraints are converging, leading to greater insights about dense matter [23]. It is hoped that GW detectors such as Advanced LIGO [1], Advanced Virgo [4], and KAGRA [34] can help constrain the nuclear EOS [29]. There have been very limited attempts at conducting parameter estimation on the nuclear EOS from rotating core collapse GW signals. Röver et al [30] used a Bayesian principal component regression model to reconstruct a rotating core collapse GW signal and matched this to the closest waveform in the Dimmelmeier et al [9] catalogue using a χ^2 -distance. The EOS of the injected signal was classified as the EOS of the best matching catalogue signal. The lack of success in making statistical inferences about the nuclear EOS may perhaps be partly due to the notion that it has very little influence on the GW signal [9, 29]. However, in this paper, we demonstrate that it is possible to correctly identify the nuclear EOS at least approximately two thirds of the time.

Richers et al [29] provide the most in-depth study of the EOS effect on rotating core collapse and

bounce GW signal and find that the signal is largely independent of the EOS. However, the signal can see stronger dependence in the post-bounce proto-neutron star (PNS) oscillations in terms of the peak GW frequency. They find that its primary affect on the GW signal is through its effect on the mass of the inner core at bounce and the central density of the post-bounce oscillations. We use this waveform catalogue (publicly available through zenodo.org [28]), which contains 18 different nuclear EOS, and we re-frame the problem as an 18-class image classification problem, and use a deep learning algorithm called the convolutional neural network (CNN) to solve [16].

Deep learning has already seen much success in the field of GW astronomy. CNNs in particular have been used for classification and identification problems, and much of the early literature focuses on the glitch classification problem. For example, Zevin et al [35] created the **Gravity Spy** project which uses CNNs to classify glitches in Advanced LIGO data, with image labels outsourced to citizen scientists. George et al [15] improve on this by using deep transfer learning with pretrained images to get an accuracy of 98.8%. In terms of the GW signal identification problem, Gabbard et al [12] use CNNs to identify between binary black hole signals and noise, reproducing sensitivities achieved by matched-filtering. George and Huerta [14] use a CNN method called Deep Filtering to identify binary black hole signals in noise. They also use this to conduct parameter estimation. Further, Dreissigacker et al [10] use CNNs to search for continuous waves from unknown spinning neutron stars.

Much effort has gone into computing low-latency Bayesian posteriors for binary black hole systems with deep learning, particularly through the use of variational autoencoders. Gabbard et al [13] train conditional variational autoencoders to generate Bayesian posteriors around six orders of magnitude faster than any other method. Green et al [19] use conditional variational autoencoders in conjunction with autoregressive normalizing flows and demonstrate consistent results to standard Markov chain Monte Carlo (MCMC) methods, but with near-instantaneous computation time. Green and Gair [18] then generalize this further to estimate posteriors for the signal parameters of GW150914. Chua and Vallisneri [8] use multilayer perceptrons to compute one and two dimensional marginalized

Bayesian posteriors. Shen et al [32] use Bayesian neural networks to constrain parameters of binary black holes before and after merger, as well as inferring final spin and quasi-normal frequencies.

Deep learning recently began populating the core collapse GW literature. Astone et al [5] trained phenomenological g -mode models with CNNs to search for core collapse supernovae GWs in multiple terrestrial detectors. They demonstrated that their CNN can enhance detection efficiency and outperforms Coherent Wave Burst (cWB) at various signal-to-noise ratios. Iess et al [20] implement two CNNs (one on time series data, and one on spectrogram data) to classify between core collapse GW signals and noise glitches, achieving an accuracy of $\sim 95\%$. They also demonstrate a proof-of-concept to classify between multiple different waveform models, achieving an accuracy of just below $\sim 90\%$. Chan et al [6] train a CNN to classify between the neutrino explosion mechanism and magnetorotational explosion mechanism in the time-domain. They only tested the performance of the CNN on four signals, but achieved a true alarm probability up to $\sim 83\%$ for magnetorotational signals at 60 kpc and up to $\sim 93\%$ for neutrino-driven signals at 10 kpc, with a fixed false alarm probability of 10%.

In this paper, we train a CNN with 11 layers to explore patterns in the rotating core collapse GW signal images and make predictions about the nuclear EOS in previously unseen test images. The output of the network is a vector of 18 probabilities for each image. The EOS class with the highest probability is the predicted EOS. We can think of it as the “most likely” EOS predicted for that GW signal. We can predict the EOS with 71% accuracy. If we then consider the five most likely EOS, the signal will be correctly identified with 97% accuracy.

The paper is outlined as follows. In Section II, we describe key elements of deep learning and discuss the convolutional neural network (CNN) architecture used in this paper. This is followed by a description of the data and the preprocessing required to convert it into appropriate input images in Section III. We then present results and discussion in Section IV and concluding remarks in Section V.

II. DEEP CONVOLUTIONAL NEURAL NETWORKS

The primary objective in machine learning is to learn patterns and rules in *training* data in order to make accurate predictions about previously unseen *test* data. *Deep learning* is an area of machine learning that transforms input data using multiple *layers* that progressively learn more meaningful representations of the data [16]. Each layer mathematically transforms its input data into an output called a *feature map*. The final step of each layer is to calculate the values of the feature map using a non-linear *activation function*. The feature map of one layer is the input of the next layer, allowing us to sequentially stack a network together.

One of the most popular deep learning methods, particularly in the realm of computer vision and image classification, is the *convolutional neural network* (CNN) [7]. Inputs into CNNs are usually 2D images, and the primary objective is to predict the label (or class) of each image. Feature maps in CNNs are usually 3D tensors with two spatial axes (height and width) and one axis that determines the *depth* of the layer. These determine the number of trainable parameters in each layer. Colour images (as inputs into CNNs) have depth 3 when using the RGB colour space; one channel each for red, green, and blue. These can be transformed through successive layers into feature maps with arbitrary depths, which encode more abstract features than the three colour channels. We can therefore think of each layer as applying filters to its input to create a feature map.

At the final layer, we get a prediction, \hat{y} . In the context of image classification \hat{y} will be a probability mass function across all the image classes, $c = 1, 2, \dots, C$. This output is compared to the truth y , which in image classification is a Kronecker delta function (i.e., 1 for the true class and 0 otherwise). A distance between y and \hat{y} computed using a *loss function* that measures how well the algorithm has performed when making its prediction. The key step in deep learning is to feed this information back through the layers in order to tune the network's parameters. This involves using the *backpropagation* algorithm which implements an optimization routine to minimize the loss function, and often uses various forms of stochastic gradient descent and the chain rule.

CNNs use three different types of layers stacked

together to create a network architecture. These are convolutional layers, pooling layers, and fully-connected layers. In the first instance, a convolutional layer will apply the convolution operation to learn abstract local patterns (such as edges) in images by considering small 2D sliding windows, producing an output feature map (of specified depth). Additional convolutional layers (with the previous layers' feature map as input) then allow us to progressively learn larger patterns in the spatial hierarchy (such as specific parts of objects) [7].

Pooling layers reduce the number of trainable parameters in a CNN by aggressively downsampling feature maps, i.e., clustering neighbouring locations of the input together using a summary statistic. In the case of max-pooling, the maximum value from each cluster is taken. Pooling produces feature maps that are approximately translation invariant to local changes in an input [16].

It is often easiest to think of convolutional and pooling layers in terms of the feature map shape (or tensor dimensions) they output, however, fully-connected layers are best considered in terms of neurons. Each neuron may have many inputs (x_1, x_2, \dots, x_n) and one output y . Each input has a weight (w_1, w_2, \dots, w_n) and a neuron may have bias w_0 associated with another input $x_0 = 1$ [25]. The weights and bias are thought of as the (tunable) parameters of each neuron. The neuron is *activated* by computing the linear combination of the inputs and weights/biases (i.e., linear activation). It is then fed into a non-linear activation function $f(\cdot)$ to compute its output y . That is,

$$a = \sum_{i=0}^n w_i x_i, \quad (1)$$

$$y = f(a). \quad (2)$$

A fully-connected layer connects one layer of neurons to another. If there are n input neurons and m output neurons, the number of tuneable parameters for that layer will be $(n + 1) \times m$.

Perhaps the most challenging issue with fitting CNNs is the potential for over-fitting as there can be millions of network parameters, and the algorithm may only memorize patterns in the *training set* and not be able to generalize these to previously unseen data presented in the *test set*. This is why it is important to monitor and tune a network using a *validation set*.

In this paper, we implement an 11 layer CNN. The 11 layers of the network architecture is outlined in Table I and is visualized in Figure 1. The input layer is a 3D tensor (image) with two spatial axes (width and height) and a depth axis of either one (for grayscale) or three (for RGB). Each convolution layer will use windows of (3×3) windows (with stride 1) and each max-pooling layer will downsample by a factor of 2. At the 9th layer, we “flatten” the output feature map from the 8th layer to a 1D vector with the same number of neurons, which then allows us to use fully-connected layers, connecting each neuron in the current layer to neurons in the previous one.

TABLE I: The CNN architecture. We use 11 layers, first sequencing between convolution and max-pooling layers of increasing depth. The Output Shape column is written as a 3D tensor with indices (Height, Width, Depth). We then flatten the output tensor from the 8th layer into a 1D vector, followed by two fully-connected layers. It is easier to think of fully-connected layers in terms of the number of output neurons. The final output is a probability mass function for the $C = 18$ different EOS classes.

Layer	Type	Output Shape	Activation
0	Input	(256, 256, 3)	
1	Convolution	(256, 256, 32)	ReLU
2	Max-Pooling	(128, 128, 32)	
3	Convolution	(128, 128, 64)	ReLU
4	Max-Pooling	(64, 64, 64)	
5	Convolution	(64, 64, 128)	ReLU
6	Max-Pooling	(32, 32, 128)	
7	Convolution	(32, 32, 128)	ReLU
8	Max-Pooling	(16, 16, 128)	
Layer	Type	# Output Neurons	Activation
9	Flatten	32768	
10	Fully-Connected	512	ReLU
11	Fully-Connected	18	Softmax

The rectified linear unit (ReLU) is a non-linear activation function used on many of the layers in the network and is defined as

$$f(x) = \max(0, x). \quad (3)$$

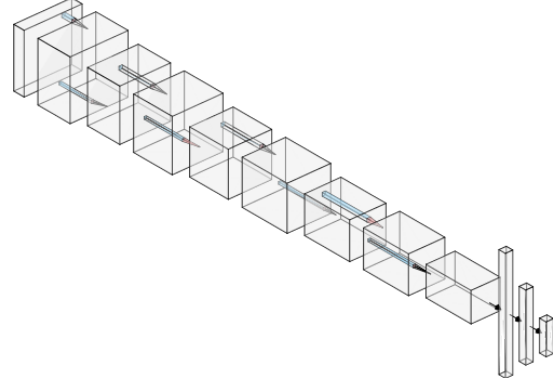


FIG. 1: The CNN architecture visualized. The feature map (output) produced by each layer is the input into the next layer. Convolution and pooling layers get progressively deeper. The height and width of the feature maps become smaller through pooling.

The softmax function is used as the final activation, the output of which is an 18-dimensional vector of probabilities for each image. This is defined as

$$\hat{p}_i^{(c)} = \frac{\exp(w_c^T x)}{\sum_{c=1}^C \exp(w_c^T x)}, \quad c = 1, 2, \dots, C, \quad (4)$$

where x is the feature map from the previous layer, w_c is the vector of weights connecting the the output from the previous layer to class c , and $C = 18$ as we have 18 different EOS we are classifying, and $(\hat{p}_i^{(1)}, \hat{p}_i^{(2)}, \dots, \hat{p}_i^{(C)})$ is the vector of probabilities for the i^{th} image.

The loss function that we minimize is the *categorical cross-entropy*, which is commonly-used throughout multi-class classification problems. This is defined as

$$L(p, \hat{p}) = - \sum_{i=1}^N \sum_{c=1}^C p_i^{(c)} \log \hat{p}_i^{(c)}, \quad (5)$$

where N is the number of images in the training set and

$$p_i^{(c)} = \begin{cases} 1 & \text{if image } i \text{ belongs to class } c, \\ 0 & \text{otherwise.} \end{cases} \quad (6)$$

We use the **RMSProp** optimizer as our gradient descent routine. The CNN is implemented in **Python** using the **Keras** deep learning framework [7].

III. PREPROCESSING

We use the 1824 simulated rotating core collapse GW signals of Richers et al [29], and the data is publicly available at [28].

Each signal in the data set has a source distance of 10 kpc from Earth. The data is originally sampled at 65535 Hz. We downsample the data to 4096 Hz as the maximum peak frequency in Richers et al [29] is 1051.4 Hz and according to Shannon-Nyquist theorem, we need to sample at least two times the maximum frequency we wish to resolve. We round up to the nearest base-2 frequency to utilize the speed and efficiency of the fast Fourier transform (FFT).

Before downsampling, we first multiply the time-domain data by a Tukey window with tapering parameter $\alpha = 0.1$ to mitigate spectral leakage, and apply a low-pass Butterworth filter (with order 10 and attenuation 0.25) to prevent aliasing. We then downsample by removing data according to the algorithm outlined by Smith and Gossett [33].

We align all signals such that $t_b = 0$, where t_b is the time of core bounce, and restrict our attention to the signal at times $t \in [t_b - 0.05 \text{ s}, t_b + 0.075 \text{ s}]$, as this is where the most interesting dynamics of the GW signal occur.

No noise (simulated or real) is added to the signal in this paper as our primary goal is to explore the GW signal dependence on the nuclear EOS.

We need to produce the images to feed into the CNN. We explore the data in three different ways; in the time-domain with the time series signal, in the frequency-domain with the periodogram (squared modulus of Fourier coefficients), and in time-frequency space with a spectrogram.

First, we create images of the time-domain data. We transform the data set so all signals are on the unit interval. We translate all signals by subtracting the minimum strain in the entire data set, and then rescale by dividing by the maximum strain in the entire data set. We plot the data, making sure to remove the axes, scales, ticks, and labels, as these will add unwanted noise in the image. We then save each image as a (256×256) pixel image in **jpeg** format. An example of one of these time series images is illustrated in Figure 2.

The second set of images are the periodograms of the GW signals. The squared modulus of the Fourier coefficients is computed and then transformed to the unit interval by translating and rescaling as before.

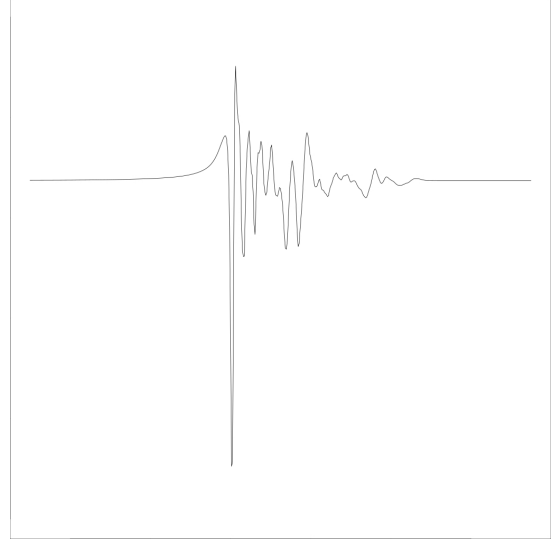


FIG. 2: 256×256 pixel image of the time series of the 670th signal in the Richers et al [29] catalogue. This signal has the HShen EOS.

The resulting frequency-domain representations are plotted (on the \log_{10} scale) and saved in **jpeg** format as before. The periodogram of the signal presented in Figure 2 is displayed in Figure 3.

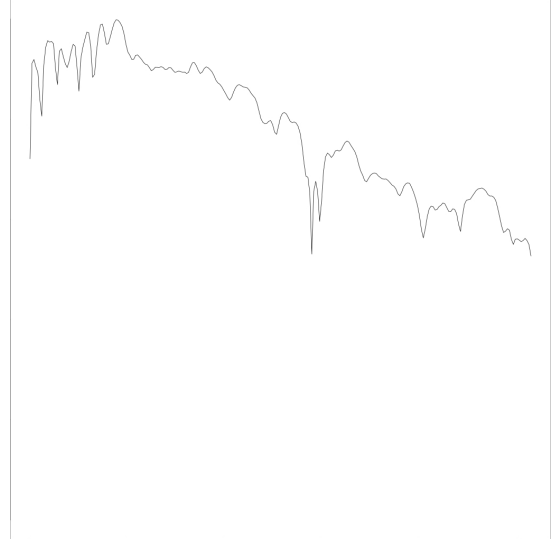


FIG. 3: 256×256 pixel image of the periodogram of the 670th signal in the Richers et al [29] catalogue. This signal has the HShen EOS.

The third set of images are time-frequency maps of the data. We generate the (256×256 pixel jpeg) images by computing and plotting the spectrogram, which represents a signal’s power content over time and frequency. We use a window length of 2^7 , an overlap of 99%, and Tukey tapering parameter $\alpha = 0.01$.

An example image used as input into the algorithm is presented in Figure 4. Note that the frequency axis is on the \log_2 scale, and power (colour) is normalized by dividing the power in each of the spectrograms by the maximum total power in the catalogue to ensure images are all on the same scale. As before, axes, ticks, scales, and labels are removed.

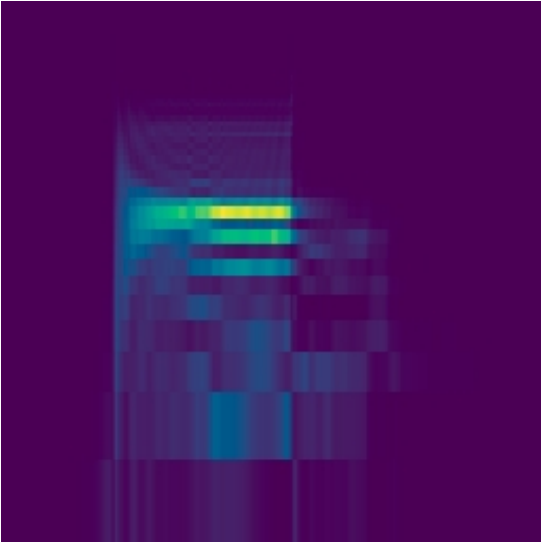


FIG. 4: 256×256 image of the spectrogram of the 670th signal in the Richers et al [29] catalogue. This signal has the HShen EOS.

We then randomly shuffle the spectrogram images such that $\sim 70\%$ are in the training set ($n_{\text{training}} = 1302$), $\sim 15\%$ are in the validation set ($n_{\text{validation}} = 261$), and $\sim 15\%$ are in the test set ($n_{\text{test}} = 261$).

We run three separate CNNs (one each for the time series images, periodogram images, and spectrogram images) to explore visual patterns with the goal of classifying nuclear EOS.

The input depth for the time series and periodogram images is one grayscale colour channel, whereas for the spectrogram images, this is a three colour RGB channel.

IV. RESULTS

We measure the success of the three CNNs in terms of the proportion of test signals that have the correct EOS classification, called the *accuracy* of the network. In this study, we achieve 64% accuracy for the spectrogram images, 65% for the periodogram images, and 71% for the time series images.

State-of-the-art CNNs can achieve accuracies of up to 95-99% on every-day objects in computer vision competitions such as those based on the ImageNet database [31]. This has been demonstrated effectively the GW literature (see e.g., [15]). Though our achieved accuracy of 64-71% is lower than this, it is much higher than anticipated. As noted by Richers et al [29], the rotating core collapse GW signal has only very weak dependence on nuclear EOS. Our results suggest that this could be upgraded to “moderate” dependence. What is also surprising is the algorithm achieved this accuracy with a relatively small training data set ($n = 1302$).

Let us now consider the “top 5” EOS classifications for each image. That is, the five EOS classes with the highest probabilities for each image. We compute the cumulative proportion images in the test set that are correctly classified within these top 5 classes. The cumulative proportion of correct classifications can be seen in Table II. Interestingly, the CNN trained on time series images outperforms the others. For each CNN, the EOS class with the second highest probability is the correct classification on more than 10% of the test signals, indicating that we can correctly classify the EOS within the top 2 classes 75-84% of the time. For the time series CNN, we achieve 90% correct classifications within the top 3 EOS classes. We can correctly constrain the nuclear EOS to one in five classes (rather than one in 18) 97%, 93%, and 91% of the time for the time series CNN, periodogram CNN, and spectrogram CNN respectively. These results are encouraging and demonstrate that we can constrain the nuclear EOS with reasonable accuracy.

We run the CNN in batches of size 32 for 100 epochs, making sure to monitor validation accuracy and loss. Surprisingly, over-fitting was not an issue with this data set, even though it is relatively small. No regularization, drop-out, or K -fold validation was required. While training accuracy tended towards 100% as the number of epochs increased, validation accuracy remained reasonably constant at

TABLE II: Cumulative proportion of correct classifications.

	Time Series	Periodogram	Spectrogram
1	0.71	0.65	0.64
2	0.85	0.77	0.75
3	0.91	0.85	0.83
4	0.93	0.90	0.85
5	0.97	0.93	0.91

60–70% after about 40 epochs, and this translated to the test set.

V. CONCLUSIONS

This paper demonstrated a proof-of-concept that rotating core collapse GW signals moderately depend on the nuclear EOS. We are encouraged by the 71% correct classifications achieved when using the CNN framework to probe visual patterns in rotating core collapse GW signals. We are further encouraged

by the 91–97% correct classifications after considering the five EOS classes with the highest estimated probability for each test signal. With this in mind, we plan a follow-up study to explore further how the feature maps of each layer can help understand exactly how each nuclear EOS influences the GW signal.

The goal of this paper was not to conduct parameter estimation in the presence of noise, but more to explore the dependence a rotating core collapse GW signal has on the nuclear EOS. However, this is a goal of a future project, where we aim to add real or simulated detector noise to see if we can constrain nuclear EOS under more realistic settings.

The deep learning framework is becoming a force of its own in the GW data analysis literature; allowing for near-instantaneous low-latency Bayesian posterior computations using pre-trained networks, producing accurate and efficient GW signal and glitch classifications, and allowing us to solve problems previously thought impossible.

ACKNOWLEDGEMENTS

The author would like to thank Nelson Christensen and Ollie Burke for fruitful discussions.

-
- [1] Aasi J, et al (2015) Advanced LIGO. Classical and Quantum Gravity 32(7):074,001, doi:10.1088/0264-9381/32/7/074001, URL <https://doi.org/10.1088/0264-9381/32/7/074001>
 - [2] Abbott B, et al (2020) Optically targeted search for gravitational waves emitted by core-collapse supernovae during the first and second observing runs of Advanced LIGO and Advanced Virgo. Phys Rev D 101:084,002, doi:10.1103/PhysRevD.101.084002, URL <https://link.aps.org/doi/10.1103/PhysRevD.101.084002>
 - [3] Abdikamalov E, Gossan S, DeMaio AM, Ott CD (2014) Measuring the angular momentum distribution in core-collapse supernova progenitors with gravitational waves. Physical Review D 90:044,001
 - [4] Acernese F, et al (2014) Advanced Virgo: a second-generation interferometric gravitational wave detector. Classical and Quantum Gravity 32(2):024,001, doi:10.1088/0264-9381/32/2/024001, URL <https://doi.org/10.1088/0264-9381/32/2/024001>
 - [5] Astone P, Cerdá-Durán P, Di Palma I, Drago M, Muciaccia F, Palomba C, Ricci F (2018) New method to observe gravitational waves emitted by core collapse supernovae. Phys Rev D 98:122,002, doi:10.1103/PhysRevD.98.122002, URL <https://link.aps.org/doi/10.1103/PhysRevD.98.122002>
 - [6] Chan ML, Heng I, Messenger C (2019) Detection and classification of supernova gravitational waves signals: A deep learning approach. arXivorg URL <http://search.proquest.com/docview/2331700621/>
 - [7] Chollet F (2018) Deep Learning with Python. Manning Publications Co., Shelter Island, New York
 - [8] Chua AJK, Vallisneri M (2020) Learning Bayesian posteriors with neural networks for gravitational-wave inference. Phys Rev Lett 124:041,102, doi:10.1103/PhysRevLett.124.041102, URL <https://link.aps.org/doi/10.1103/PhysRevLett.124.041102>
 - [9] Dimmelmeier H, Ott CD, Marek A, Janka HT (2008) The gravitational wave burst signal from core collapse of rotating stars. Physical Review D 78:064,056
 - [10] Dreissigacker C, Sharma R, Messenger C, Zhao R, Prix R (2019) Deep-learning con-

- tinuous gravitational waves. *Phys Rev D* 100:044,009, doi:10.1103/PhysRevD.100.044009, URL <https://link.aps.org/doi/10.1103/PhysRevD.100.044009>
- [11] Edwards MC, Meyer R, Christensen N (2014) Bayesian parameter estimation of core collapse supernovae using gravitational wave simulations. *Inverse Problems* 30(11), doi:10.1088/0266-5611/30/11/114008
- [12] Gabbard H, Williams M, Hayes F, Messenger C (2018) Matching matched filtering with deep networks for gravitational-wave astronomy. *Phys Rev Lett* 120:141,103, doi:10.1103/PhysRevLett.120.141103, URL <https://link.aps.org/doi/10.1103/PhysRevLett.120.141103>
- [13] Gabbard H, Messenger C, Heng IS, Tonolini F, Murray-Smith R (2019) Bayesian parameter estimation using conditional variational autoencoders for gravitational-wave astronomy. arXiv:1909.06296 [astro-ph.IM]
- [14] George D, Huerta E (2018) Deep learning for real-time gravitational wave detection and parameter estimation: Results with Advanced LIGO data. *Physics Letters B* 778:64 – 70, doi: <https://doi.org/10.1016/j.physletb.2017.12.053>, URL <http://www.sciencedirect.com/science/article/pii/S0370269317310390>
- [15] George D, Shen H, Huerta EA (2018) Classification and unsupervised clustering of LIGO data with deep transfer learning. *Phys Rev D* 97:101,501, doi:10.1103/PhysRevD.97.101501, URL <https://link.aps.org/doi/10.1103/PhysRevD.97.101501>
- [16] Goodfellow I, Bengio Y, Courville A (2016) *Deep Learning*. The MIT Press
- [17] Gossan SE, Sutton P, Stuver A, Zanolin M, Gill K, Ott CD (2016) Observing gravitational waves from core-collapse supernovae in the advanced detector era. *Phys Rev D* 93:042,002, doi:10.1103/PhysRevD.93.042002, URL <https://link.aps.org/doi/10.1103/PhysRevD.93.042002>
- [18] Green SR, Gair J (2020) Complete parameter inference for gw150914 using deep learning. arXiv:2008.03312 [astro-ph.IM]
- [19] Green SR, Simpson C, Gair J (2020) Gravitational-wave parameter estimation with autoregressive neural network flows. arXiv:2002.07656 [astro-ph.IM]
- [20] Iess A, Cuoco E, Morawski F, Powell J (2020) Core-collapse supernova gravitational-wave search and deep learning classification. *Machine Learning: Science and Technology* 1(2):025,014, doi:10.1088/2632-2153/ab7d31, URL <https://doi.org/10.1088/2632-2153/ab7d31>
- [21] Janka HT (2012) Explosion mechanisms of core-collapse supernovae. *Annual Review of Nuclear and Particle Science* 62(1):407–451, doi:10.1146/annurev-nucl-102711-094901, URL <https://doi.org/10.1146/annurev-nucl-102711-094901>
- [22] Kuroda T, Kotake K, Hayama K, Takiwaki T (2017) Correlated signatures of gravitational-wave and neutrino emission in three-dimensional general-relativistic core-collapse supernova simulations. *The Astrophysical Journal* 851(1):62, doi:10.3847/1538-4357/aa988d, URL <https://doi.org/10.3847/1538-4357/aa988d>
- [23] Lattimer JM (2012) The nuclear equation of state and neutron star masses. *Annual Review of Nuclear and Particle Science* 62(1):485–515, doi:10.1146/annurev-nucl-102711-095018, URL <https://doi.org/10.1146/annurev-nucl-102711-095018>
- [24] Logue J, Ott CD, Heng I, Kalmus P, Scargill JHC (2012) Inferring core-collapse supernova physics with gravitational waves. *Phys Rev D* 86:044,023, doi:10.1103/PhysRevD.86.044023, URL <https://link.aps.org/doi/10.1103/PhysRevD.86.044023>
- [25] MacKay DJC (2003) *Information Theory, Inference, and Learning Algorithms*. Cambridge University Press, USA
- [26] Powell J, Gossan SE, Logue J, Heng IS (2016) Inferring the core-collapse supernova explosion mechanism with gravitational waves. *Phys Rev D* 94:123,012, doi:10.1103/PhysRevD.94.123012, URL <https://link.aps.org/doi/10.1103/PhysRevD.94.123012>
- [27] Powell J, Szczepanczyk M, Heng IS (2017) Inferring the core-collapse supernova explosion mechanism with three-dimensional gravitational-wave simulations. *Phys Rev D* 96:123,013, doi:10.1103/PhysRevD.96.123013, URL <https://link.aps.org/doi/10.1103/PhysRevD.96.123013>
- [28] Richers S, Ott CD, Abdikamalov E, O’Connor E, Sullivan C (2016) Equation of State Effects on Gravitational Waves from Rotating Core Collapse. doi:10.5281/zenodo.201145, URL <https://doi.org/10.5281/zenodo.201145>
- [29] Richers S, Ott CD, Abdikamalov E, O’Connor E, Sullivan C (2017) Equation of state effects on gravitational waves from rotating core collapse. *Phys Rev D* 95:063,019, doi:10.1103/PhysRevD.95.063019, URL <https://link.aps.org/doi/10.1103/PhysRevD.95.063019>
- [30] Röver C, Bizouard MA, Christensen N, Dimmelmeier H, Heng I, Meyer R (2009) Bayesian reconstruction of gravitational wave burst sig-

- nals from simulations of rotating stellar core collapse and bounce. *Physical Review D - Particles, Fields, Gravitation and Cosmology* 80(10), doi: 10.1103/PhysRevD.80.102004
- [31] Russakovsky O, Deng J, Su H, Krause J, Satheesh S, Ma S, Huang Z, Karpathy A, Khosla A, Bernstein M, Berg AC, Fei-Fei L (2015) ImageNet Large Scale Visual Recognition Challenge. *International Journal of Computer Vision (IJCV)* 115(3):211–252, doi:10.1007/s11263-015-0816-y
- [32] Shen H, Huerta EA, Zhao Z, Jennings E, Sharma H (2019) Deterministic and Bayesian neural networks for low-latency gravitational wave parameter estimation of binary black hole mergers. arXiv:190301998 [gr-qc]
- [33] Smith J, Gossett P (1984) A flexible sampling-rate conversion method. In: ICASSP '84. IEEE International Conference on Acoustics, Speech, and Signal Processing, vol 9, pp 112–115
- [34] Somiya K (2012) Detector configuration of KAGRA—the japanese cryogenic gravitational-wave detector. *Classical and Quantum Gravity* 29(12):124,007, doi:10.1088/0264-9381/29/12/124007, URL <https://doi.org/10.1088%2F0264-9381%2F29%2F12%2F124007>
- [35] Zevin M, Coughlin S, Bahaadini S, Besler E, Rohani N, Allen S, Cabero M, Crowston K, Katsaggelos AK, Larson SL, Lee TK, Lintott C, Littenberg TB, Lundgren A, Østerlund C, Smith JR, Trouille L, Kalogera V (2017) Gravity Spy: integrating Advanced LIGO detector characterization, machine learning, and citizen science. *Classical and Quantum Gravity* 34(6):064,003, doi:10.1088/1361-6382/aa5cea, URL <https://doi.org/10.1088%2F1361-6382%2Faa5cea>